Statistical Analysis of the Spatial Evolution of the Stationary Wind Wave Field

A. ZAVADSKY

School of Mechanical Engineering, Tel-Aviv University, Tel-Aviv, Israel

D. LIBERZON

Civil Engineering and Geological Sciences, University of Notre Dame, Notre Dame, Indiana

L. SHEMER

School of Mechanical Engineering, Tel-Aviv University, Tel-Aviv, Israel

(Manuscript received 14 June 2012, in final form 16 August 2012)

ABSTRACT

Detailed investigation of wind-generated water waves in a 5-m-long wind wave flume facility is reported. Careful measurements were carried out at a large number of locations along the test section and at numerous airflow rates. The evolution of the wind wave field was investigated using appropriate dimensionless parameters. When possible, quantitative comparison with the results accumulated in field measurements and in larger laboratory facilities was performed. Particular attention was given to the evolution of wave frequency spectra along the tank, distinguishing between the frequency domain around the spectral peak and the high-frequency tail of the spectrum. Notable similarity between the parameters of the evolving wind wave field in the present facility and in field measurements was observed.

1. Introduction

Sea surface waves generated by wind are random and thus have to be described in statistical terms. Modern theoretical analysis of wave statistics was initiated by Longuet-Higgins (1952) who showed that if the temporal variation of the surface elevation can be described by a narrow-banded Gaussian frequency spectrum, the wave heights follow the Rayleigh distribution. One of the first field studies of sea waves by Kinsman (1965) showed that the distribution of surface elevation, although skewed owing to the wave nonlinearity, have shape that is close to Gaussian, while the waves' heights have exceedance probabilities that approximately follow Rayleigh distribution. It was also demonstrated that the probability distribution of the highest waves may deviate notably from the predictions based on the Rayleigh distribution. The knowledge of probability of steepest waves for a given wave state is of great practical importance for marine traffic and offshore engineering. Forristall (1978) reported that Rayleigh distribution overestimates the probability of high waves owing to their nonlinearity, while Tayfun (1980) attributes this discrepancy to wave breaking. For more recent statistical studies of wave height distribution in nonlinear wave field see, for example, Forristall (2005), Tayfun and Fedele (2007), and references therein.

Extensive experimental studies of statistics of mechanically excited unidirectional random water waves carried out in large wave tanks by Socquet-Juglard et al. (2005), Onorato et al. (2005, 2006), Mori et al. (2007), Shemer and Sergeeva (2009), and Shemer et al. (2010a,b), demonstrated significant deviations from the Gaussian behavior that were shown to be dependent on wave nonlinearity and spectral width. In these studies the evolution along the tank of the statistical parameters characterizing the wave field was investigated. The effect of the directional spreading was in the focus of large wave basin experiments by Onorato et al. (2009). In all these studies no wave energy was introduced to the wave field once the waves were generated by the wavemaker. Since the effects of dissipation were of relatively minor importance, the waves in those experiments constituted an essentially conservative system. Spatial evolution of

Corresponding author address: L. Shemer, School of Mechanical Engineering, Tel-Aviv University, Tel-Aviv, Israel.
E-mail: shemer@eng.tau.ac.il

DOI: 10.1175/JPO-D-12-0103.1

the wave field statistics thus resulted nearly solely from the nonlinear interactions among waves.

Wind waves in general, and in a laboratory tank in particular, represent a qualitatively different wave system. Not only energy and momentum are transferred from wind to waves everywhere in the wave field, the dissipation, mainly because of breaking, in general cannot be neglected. The energy input and the energy sink are distributed nonuniformly among the wave frequencies and may be more prominent at different spectral ranges. Thus, the evolution of the statistical parameters in this case is very different from the conservative case; it is mostly dependent on wind input and dissipation.

Dimensional analysis of an evolving wind wave field was first presented by Kitaigorodskii (1961). The principal statistical parameters that characterize wind wave field are the power frequency spectrum $F(\omega)$, the characteristic wave heights H that are related to the zero-order spectral momentum $m_0 = \int F(\omega)\, d\omega = \langle \eta^2 \rangle$, η being the surface elevation, and the peak radian frequency ω_p. Kitaigorodskii suggested that for a quasi-steady spatially evolving wave field these parameters, when rendered dimensionless, should satisfy the following relations:

$$g^3 F(\omega)/U^5 = f_1(U\omega/g, gx/U^2), \tag{1}$$

$$g^2 m_0/U^4 = f_2(gx/U^2), \quad \text{and} \tag{2}$$

$$U\omega_p/g = f_3(gx/U^2), \tag{3}$$

where g is the acceleration of gravity, U is the characteristic wind speed, and x is the measurement location along the wind direction (hereinafter ''fetch''). Equation (1) relates power spectra obtained at different conditions, while (2) indicates that the characteristic wave height exhibits strong dependence on the wind velocity U. Since for pure gravity waves the celerity $c = \sqrt{g/k} = g/\omega$, the relation (3) can be seen as representing the variation of the wave age c/U with the dimensionless fetch gx/U^2. Kahma (1981) and Kahma and Calkoen (1992) offered the following nondimensional spectral form $F(\omega)$ that contrary to (1) does not explicitly contain the dependence on fetch:

$$F(\omega)\omega^5/g^2 = f(U\omega/g), \tag{4}$$

arguing that it is particularly revealing for the spectral high-frequency tail shape. The dimensional analysis by Phillips (1958) suggested that at high frequencies $F(\omega) \propto \omega^{-n}$ with $n = 5$. Experimental results of Phillips (1977) seem to substantiate the $n = 5$ spectral shape. However, Toba (1973) took a closer look at the available experimental results and suggested the following expression:

$$F_T(\omega, \omega_p, \alpha_T) = \alpha_T g u_* \omega^{-4} \exp\left[-\left(\frac{\omega_p}{\omega}\right)^4\right], \tag{5}$$

where u_* is the friction velocity and $\alpha_T \approx 0.127$ is the Toba parameter. For saturation range, usually defined as $1.5\omega_p < \omega < 3.5\omega_p$, (6) reduces to

$$F(\omega) = \alpha_T g u_* \omega^{-4}. \tag{6}$$

A more general relation that accounts for energy input due to the wind–wave interaction was offered by Badulin et al. (2007). For the frequency range where nonlinear interactions are dominant and energy exchange due to the wind input and dissipation can be neglected, they suggested a $n = 4$ spectral shape. Janssen (2004) presented the following parameterization of the frequency spectrum

$$F(\omega) = F_{PM}(\omega, \omega_p, \alpha_p) \times \gamma^{\Gamma(\omega, \omega_p, \sigma)} \tag{7}$$

proposed by Joint North Sea Wave Project (JONSWAP) group (Hasselmann et al. 1980) that is generally used to describe ocean wave spectra, here

$$F_{PM}(\omega, \omega_p, \alpha_p) = \alpha_p g^2 \omega^{-5} \exp\left[-\frac{5}{4}\left(\frac{\omega_p}{\omega}\right)^4\right] \tag{8}$$

is the spectral shape of the high-frequency part suggested by Pierson and Moskowitz (1964), $\gamma^{\Gamma(\omega, \omega_p, \sigma)}$ is the shape function that mainly affects the domain around the peak frequency, and $\alpha_p \approx 0.0083$ is the Phillips (1958) parameter.

It is generally accepted that the high-frequency tail of the wave spectrum is better approximated by a ω^{-4} shape than by the Phillips ω^{-5} power law; the coefficient of proportionality is independent of the wave age.

In the present study the spectral shapes, the wave height probability distributions, as well as numerous additional statistical parameters, are investigated under carefully controlled conditions in a laboratory wind wave flume. The experiments are carried out at a number of wind velocities and at numerous fetches along the test section.

2. Experimental facility and procedure

The experiment was conducted in a laboratory wind wave flume that consists of a closed-loop wind tunnel

over a 5-m-long test section with the cross section 0.4 m by 0.5 m. The wind tunnel is equipped with large settling chambers at the inlet and at the exit of the test section. Side walls and the bottom of the test section are made of clear glass to enable flow visualization of the wave field from all directions. The test section is covered by transparent removable Perspex plates with a partially sealed slot along the center line to facilitate the sensors positioning. Water depth in the test section was kept at about 0.2 m, satisfying deep water conditions for wind wave lengths observed in this study; a flexible flap connects the bottom of the converging nozzle to the test section slightly above the mean water level height to ensure smooth airflow. A computer-controlled blower enables maximum wind speed in the test section that may exceed 15 m s^{-1}. A heat exchanger connected to an external water chiller and controlled by a temperature controller was installed in the system and helped to eliminate excessive water evaporation because of air heating in the closed system. The chiller was set to keep the air temperature independent of wind velocity and constant at 22°C.

Capacitance-type wave gauge made of 0.3 mm tantalum wires was used for measuring instantaneous surface elevation, while a 1 mm ID Pitot tube connected to a sensitive pressure transducer (MAMAC Systems, INC ^{2} PR274) with a resolution of $2.5 \cdot 10^{-5}$ Pa determined for the local mean air velocity. The sensors were supported by a carriage that was manually positioned at a desired fetch along the test section. The wave gauge was mounted on a computer-controlled vertical stage to enable its static calibration. At any given fetch and wind velocity, the calibration of the wave gauge was performed by a computer and covered the expected range of surface elevation variation. The Pitot tube was mounted on a separate accurate computer-controlled vertical stage that enabled its positioning at any prescribed height above the water surface. Temperature in the test section was monitored using the PT-100 resistance thermometer.

A high level of automation requiring minimum human intervention in conducting the experiment was achieved by the means of a LabView program that enables controlling the wind speed in the tunnel, calibration of the wave gauge before and after each measurement session, and data acquisition. For more detailed description of the experimental facility, the available instrumentation and the calibration and data acquisition procedures employed see Liberzon and Shemer (2011).

At each fetch and airflow rate characterized by the maximum wind velocity in the test section, $U_{\max}$, the instantaneous variation of the surface elevation was continuously recorded for 90 min at the sampling rate 120 Hz, thus enabling to accumulate a very large ensemble of experimental data. Measurements were carried out at 8 fetches (x = 100, 140, 180, 220, 260, 300, 340, and 380 cm), and at 9 airflow rates in the test section. Values of $U_{\max}$ and of the corresponding friction velocities, u_*, are summarized in Table 1. Methods used to determine the friction velocities from measurements of wind velocity profiles are described in Zavadsky and Shemer (2012).

TABLE 1. Experimental conditions.

$U_{\max}$ (m s^{-1})	3.3	4.4	5.5	6.6	7.7	8.9	10.0	11.2	12.3
$\overline{u}_*$ (m s^{-1})	0.17	0.22	0.32	0.41	0.50	0.57	0.66	0.84	1.28

3. Results

The frequency spectra of the surface elevation variation with time $\eta(t)$ were calculated by dividing each record into windows that contained 8192 points (duration of each window about 70 s), with 50% overlap, resulting in 94 data segments for each fetch and airflow rate. Variation with fetch of the surface elevation power spectra averaged over all windows is presented in Figs. 1a,b for two representative airflow rates.

Growth of the total wave energy along the channel is observed for all wind velocities. At each wind speed, the peak frequency decreases with fetch; comparison of Figs. 1a,b demonstrates the shift of the peak toward lower frequencies with increasing wind speed, so that for every given fetch the wavelength increases with increasing wind speed. The results of Fig. 1 are in agreement with Liberzon and Shemer (2011).

There are two routinely used definitions of the characteristic frequency of the wind wave field, the spectral peak frequency f_p and the dominant frequency f_{dom}. The dominant frequency is based on the spectral moments computed as

$$m_j = \int_{\omega_{\min}}^{\omega_{\max}} \omega^j F(\omega)\, d\omega \tag{9}$$

and is defined as

$$f_{\mathrm{dom}} = \frac{m_1}{m_0}. \tag{10}$$

Since f_{dom} is an integral quantity and thus less subject to fluctuations in the experimentally estimated wave power spectra; it represents the most robust characteristic frequency at each fetch and airflow rate. Note that in (9) the integration is carried out over the free waves domain only; in the present study this domain for each

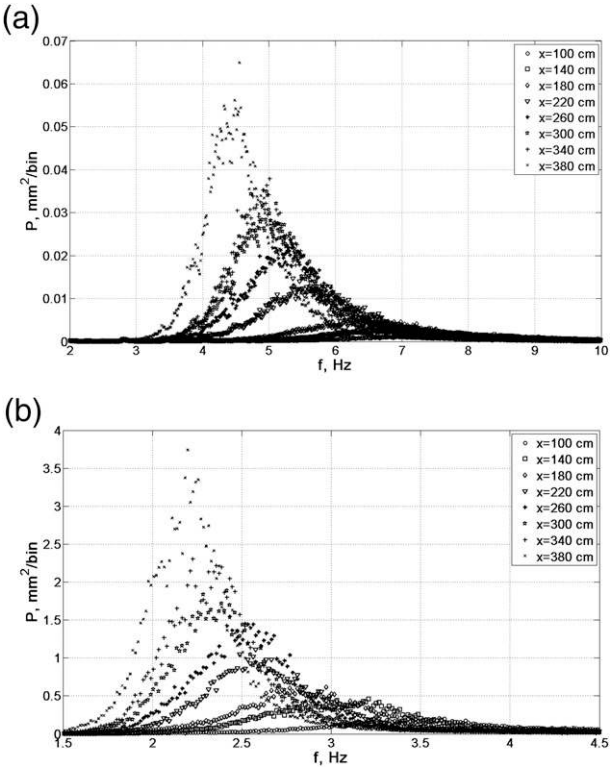

FIG. 1. Variation of surface elevation spectra along the test section: (a) $U_{\max} = 5.5$ m s^{-1} and (b) $U_{\max} = 12.3$ m s^{-1}.

spectrum $\omega_{\min} < \omega < \omega_{\max}$ is taken within $\pm 60\%$ of the peak frequency.

More often, however, the frequency of the spectral peak f_p is chosen as the characteristic of the wave field rather than f_{dom} since it constitutes a more intuitively straightforward physical and visual parameter. To mitigate the inevitable scatter in the experimentally determined power spectra, see Fig. 1, the value of f_p is defined here as the frequency of the peak of the parabolic fit performed for ± 20 data points (about ± 0.3 Hz) of the measured spectra around the corresponding maximum values.

The peak frequencies measured at all fetches and wind velocities in the present experiments are summarized in Fig. 2. As expected, the values of f_p decrease at each fetch with wind velocity; for any given wind flow rate, the peak frequency decreases with fetch.

The comparison of the values of f_{dom} and f_p is presented in Fig. 3. Although the difference between these two parameters is small, the dominant frequency is consistently larger than f_p owing to higher weight of higher frequencies in the computation of the spectral moments m_1, see (9). The linear fit that has a slope of 0.96 does not contain data points corresponding to two lowest wind flow rates; for those wind velocities the

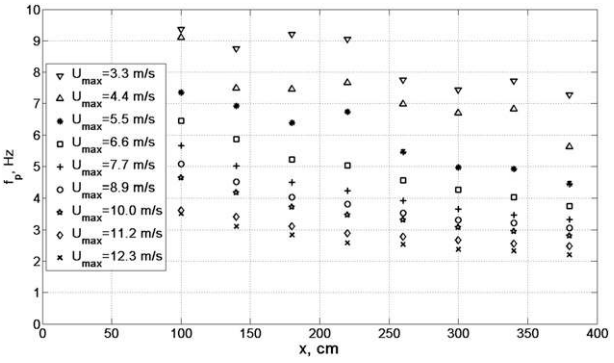

FIG. 2. Variation of the peak frequency f_p along the tank.

waves in the test section are characterized by small amplitudes and wide spectra without well-defined peaks. The peak frequency at these conditions cannot be determined with sufficient accuracy and the results exhibit considerable scatter.

The results of Fig. 2 can be presented as relations among dimensionless groups. In the present experiments the wind is steady at each fixed blower setting, the wind wave field is stationary, so that the statistical parameters depend on fetch only. The friction velocity u_* is the quantity directly related to momentum transfer from air to water and for a given airflow rate in the test section is essentially independent of fetch (Zavadsky and Shemer 2012; Liberzon and Shemer 2011). The values of u_* given in Table 1 were therefore selected as characteristic wind velocities. Equations (2) and (3) can be rewritten in a more convenient form as

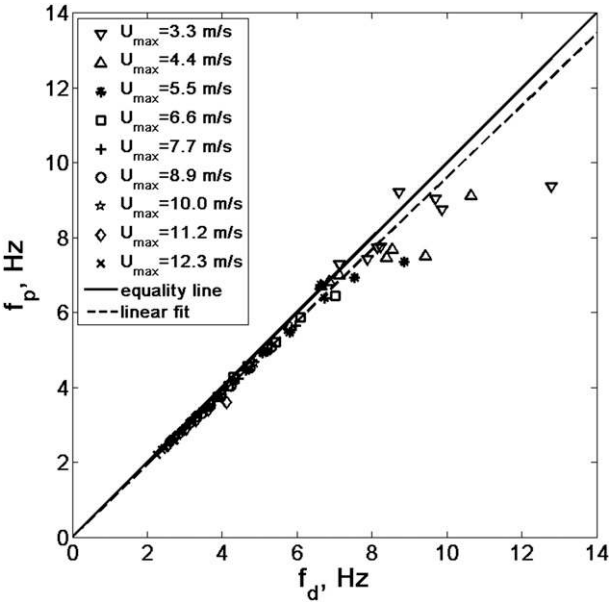

FIG. 3. Comparison of f_{dom} and f_p.

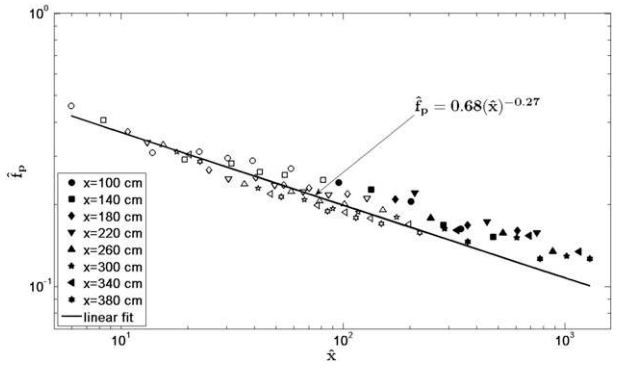

FIG. 4. Dimensionless peak frequency $\hat{f}_p$ vs dimensionless fetch $\hat{x}$.

$$\hat{\eta} = g(\overline{\eta^2})^{1/2}/u_*^2 \approx g m_0^{1/2}/u_*^2 = f_2(gx/u_*^2), \quad \text{and} \tag{11}$$

$$\hat{f}_p = u_* f_p/g = f_3(gx/u_*^2). \tag{12}$$

Note that the characteristic wave amplitude can be presented in (11) either by the rms value of the surface elevation $(\overline{\eta^2})^{1/2}$, or as based on the zero spectrum momentum m_0, see (9). The definition based on the spectral momentum seems to be advantageous as it contains free wave components only, in agreement with most nonlinear wind waves theories—see, for example, Badulin et al. (2007). The comparison of the values of $(\overline{\eta^2})^{1/2}$ and of $m_0^{1/2}$ for all experimental conditions demonstrate that wave energy is mainly contained in the spectral range around the peak frequency; the values of $m_0^{1/2}$ are smaller than the corresponding rms values of the surface elevation by less than about 3%.

Figures 4 and 5 present the measured dependence of the dimensionless peak frequency $\hat{f}_p$ and the characteristic dimensionless wave amplitude $\hat{\eta}$ on $\hat{x} = gx/u_*^2$. Note that for a given dimensional distance from the inlet x, the dimensionless fetch $\hat{x}$ decreases strongly with increased airflow rate in the tank.

The majority of points (denoted by open symbols) in Figs. 4 and 5 fit a linear dependence in log–log coordinates and thus exhibit power-law behavior. The dimensionless frequency $\hat{f}_p$ decreases with the dimensionless fetch as $\hat{x}^{-0.27}$, while the dimensionless wave amplitudes $\hat{\eta}$ grow as $\hat{x}^{0.51}$. The scatter of data represented by open symbols around the fit line can be attributed in part to local variations in the friction velocities. The power dependencies presented in Figs. 4 and 5 are in agreement with wind wave channel measurements at comparable range of dimensionless fetches by Mitsuyasu and Honda (1974) and Mitsuyasu (1968) who suggested the following relations:

$$\hat{f}_{\text{dom}} = 1.00(\hat{x})^{-0.33}, \quad \text{and} \tag{13}$$

$$\hat{m}_0^{1/2} = 1.31 \cdot 10^{-2}(\hat{x})^{0.504}, \tag{14}$$

where $\hat{m}_0^{1/2} = (g m_0^{1/2})/\overline{u}_*^2$. Similar results were obtained in field measurements by JONSWAP group (Hasselmann et al. 1980) and by Kahma (1981).

As noticed above, not all data points fit the power law pattern. Notable deviations from relations (13) and (14) were also observed by Mitsuyasu (1968) and Mitsuyasu and Honda (1974). The points in Figs. 4 and 5 that do not fit the general trend and marked by filled symbols generally correspond to the lowest wind velocities in the present experiments (and thus higher dimensionless fetches $\hat{x}$). The factors related to this abnormal behavior

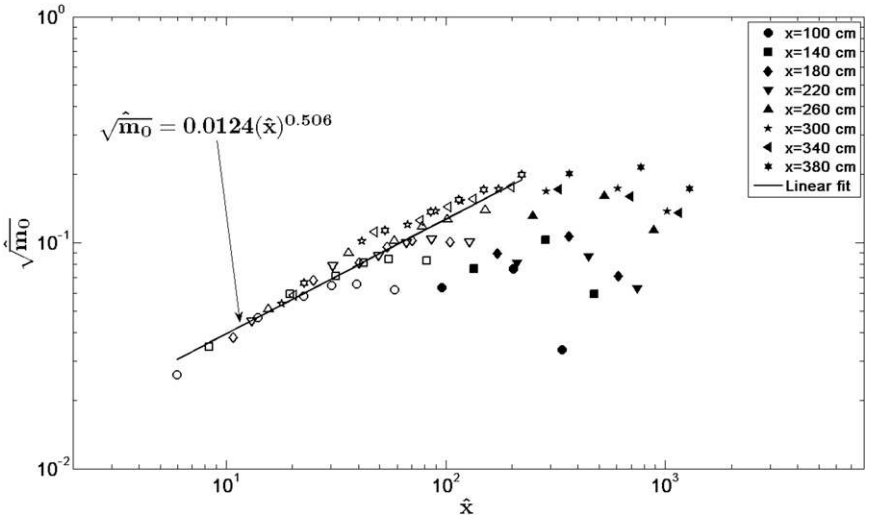

FIG. 5. Dimensionless wave amplitude $\hat{\eta}$ vs dimensionless fetch $\hat{x}$.

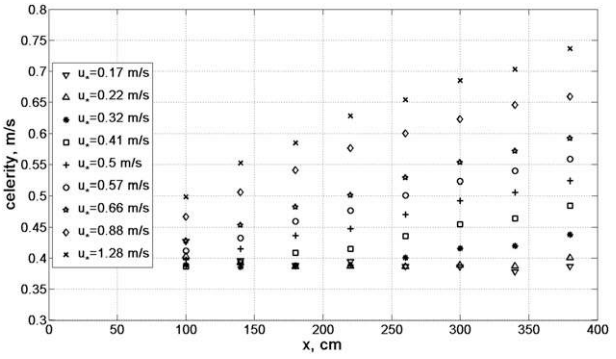

FIG. 6. Variation of the phase velocities of dominant waves along the test section.

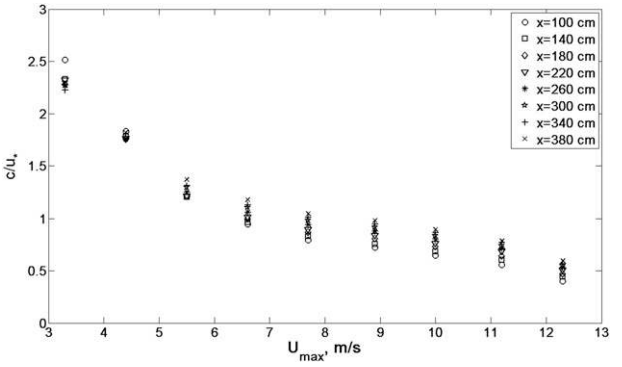

FIG. 7. Wave age vs mean wind velocity.

can be identified in Fig. 2 as well as in Fig. 6, where the peak wave phase velocity c is shown as a function of fetch. The peak frequencies at lower wind velocities mostly exceed 5 Hz at all fetches; the celerities of the corresponding short waves are strongly affected by the surface drift current (Liberzon and Shemer 2011). In these cases the wave celerities are only weakly dependent on the wave lengths and on the fetch; they are notably higher than the phase velocities of gravity–capillary waves in the absence of the current and become comparable with phase velocities of considerably longer waves characteristic for higher wind velocities. The combination of higher effective celerities with relatively low friction velocities at low flow rates results in higher wave ages c/u_*; therefore waves generated at low wind velocities appear as more mature. The variation of the wave age c/u_* with the wind velocity $U_{\max}$ in the test section is presented in Fig. 7. A moderate increase of the wave age along the test section indeed occurs at every given wind velocity. The more pronounced feature of this Figure is however the decrease of the wave age with increasing $U_{\max}$; this decrease in wave age is mostly notable at mean wind velocities below about 6–7 m s^{-1} where the wave age decreases twice when the maximum wind velocity increases from about 3 m s^{-1} to 6.5 m s^{-1}. The strong dependence of wave age on wind velocity at low airflow rates seems to cause the deviation from the power law of the energy growth and peak frequency variation along the test section; these values therefore were not included in data fits of Figs. 4 and 5. In this respect it is worth mentioning that large values of wave age at low wind speeds were also obtained in radar altimetry-based field measurements by Fu and Glazman (1991), although in this case the effect is attributed to the presence of swell.

The following relation between the dimensionless wave amplitude $\hat{m}_0^{1/2}$ and dimensionless peak frequency $\hat{f}_p$ is obtained by combining the relations given in Figs. 4 and 5.

$$\hat{m}_0^{1/2} = 0.026 \times \hat{f}_p^{-1.87}. \tag{15}$$

This result differs somewhat from the generally accepted 3/2 power law $H_s = BT_s^{3/2}$ proposed by Toba (1972) that is based on extensive empirical data; here H_s is the significant wave height and T_s defined by the peak frequency. It is customary to define H_s as the average value of 1/3 of the highest waves in the wave heights probability distribution (see, e.g., Goda 2000). The significant wave heights in the present experiments are summarized in Table 2.

The characteristic steepness of random waves ε may be defined as the product of the representative wave amplitude calculated as an rms value of the surface elevation, and the peak wavenumber $k_p = k(f_p)$; $\varepsilon = \overline{(\eta^2)}^{1/2} k_p$. Note that the wave amplitudes grow along the test section and with the wind velocity, while the values of k_p decrease with those parameters, see Figs. 4 and 5. The characteristic wave steepness ε is plotted as a function of the dimensional fetch in Fig. 8a, and as a function of the wave age in Fig. 8b. Figure 8a demonstrates that at lower wind flow rates the values of ε tend to increase with fetch; the dependence of ε on fetch subsides with the increase in $U_{\max}$. At any constant fetch, the characteristic wave steepness increases with

TABLE 2. The significant wave height H_s (mm).

	Fetch (cm)							
$U_{\max}$ (m s^{-1})	100	140	180	220	260	300	340	380
3.3	0.40	0.66	0.81	0.70	1.27	1.62	1.61	1.98
4.4	1.45	1.95	2.09	1.72	2.67	3.36	3.10	4.14
5.5	2.55	3.07	3.65	3.31	5.16	6.73	6.84	8.07
6.6	4.02	5.28	6.52	6.51	8.86	11.19	11.39	12.86
7.7	6.11	7.71	9.62	9.79	11.81	14.56	14.95	16.36
8.8	7.81	9.78	11.59	12.28	14.17	16.96	17.92	19.19
10	9.45	9.12	13.26	14.35	16.37	19.63	20.87	22.91
11.2	12.55	15.94	18.17	21.63	23.66	26.66	30.42	30.91
12.3	16.68	22.09	24.27	28.59	31.86	34.48	37.16	42.90

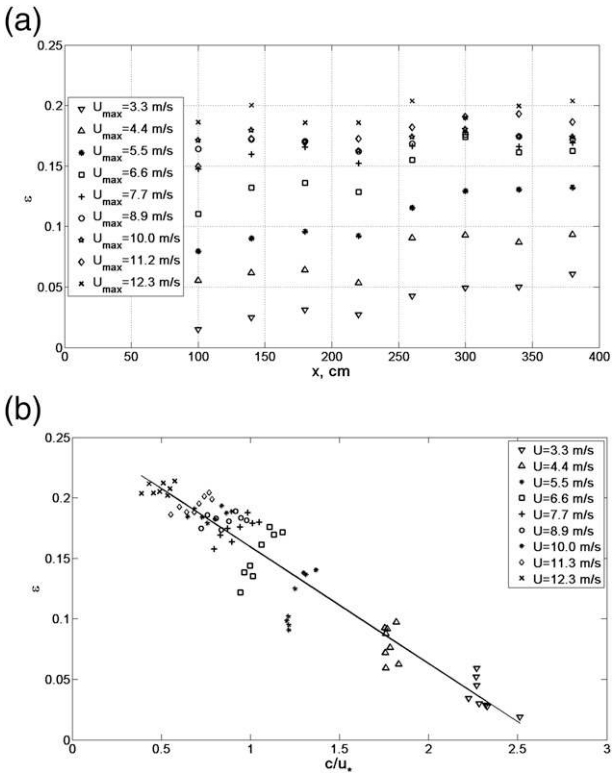

FIG. 8. The characteristic wave steepness: (a) as a function of fetch; and (b) as a function of wave age.

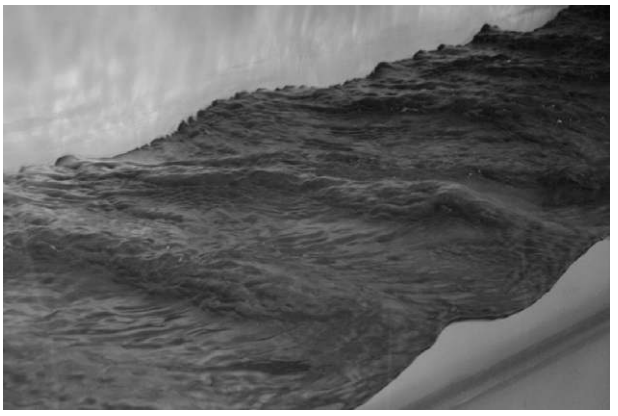

FIG. 9. Water surface state at the most severe experimental conditions (fetch around 340 cm, $U_{\max} = 11.2$ m s^{-1}).

$U_{\max}$, the growth of ε is initially fast and slows down at higher wind velocity. The results of Fig. 8a suggest that the wave steepness at all wind velocities and fetches does not notably exceed $\varepsilon = 0.2$; this value may constitute the highest possible characteristic wave steepness in a naturally evolving young wind wave field. Additional increase in wave steepness is most probably constrained by microbreaking due to appearance of short ripples as characteristic for wind waves shorter than about 30 cm—see, for example, Caulliez et al. (2008). A snapshot of the typical wave field at the far end of the test section under the strongest wind in the present experiments is shown in Fig. 9. The white-capping that characterizes breaking of longer wind waves is virtually absent, and dissipation of wave energy occurs by microbreaking that is randomly spread over the entire surface.

When plotted against the wave age, Fig. 8b, the characteristic steepness values decrease following a linear trend for the range of parameters investigated. Note the variation of the slope of the pattern for each wind flow rate in the test section, from a nearly vertical at low wind velocities, corresponding to considerable change in steepness coupled with a nearly independent of fetch wave age at these conditions, to close to horizontal for stronger winds, where the steepness remains practically constant while the wave age increases along the test section.

The surface elevation power spectra are now examined in greater detail in Fig. 10. In Fig. 10a the spectra obtained at a constant airflow rate are plotted in a logarithmic scale as a function of the dimensional frequency, whereas in Fig. 10b the power spectra for a wide range of wind velocities are normalized by their peak values and presented as a function of f/f_p. The line corresponding to the power law with $n = 4$ is also plotted in Fig. 10.

The spectra in Fig. 10 are characterized by clearly visible peaks at the second and the third harmonics of the peak frequency. At low wind velocities even weaker peaks corresponding fourth harmonic can be identified. Those peaks signify the bound waves contribution to the nonlinear wave field. At frequencies exceeding the third or the fourth harmonics of the peak frequencies, the bound waves' contributions cannot be distinguished; those frequencies correspond to the so-called quasi-saturated high-frequency tail. The normalized power spectra of the surface elevation for a range of wind flow rates in Fig. 10b seem to collapse on a single curve, as long as the frequency is below about $3f_p$. The tail behavior is only in a qualitative agreement with the $n = 4$ slope; notable spread of the tail slopes is clearly visible in Fig. 10b.

The dimensionless spectral width ν identified by the spectral moments given by (9) as

$$\nu = \sqrt{\frac{m_0 m_2}{m_1^2} - 1} \tag{16}$$

constitutes an integral characteristic of the shape of the free wave part of the power spectrum. The values of ν calculated for all airflow rates and fetches in the present experiment are plotted in Fig. 11. For each airflow rate,

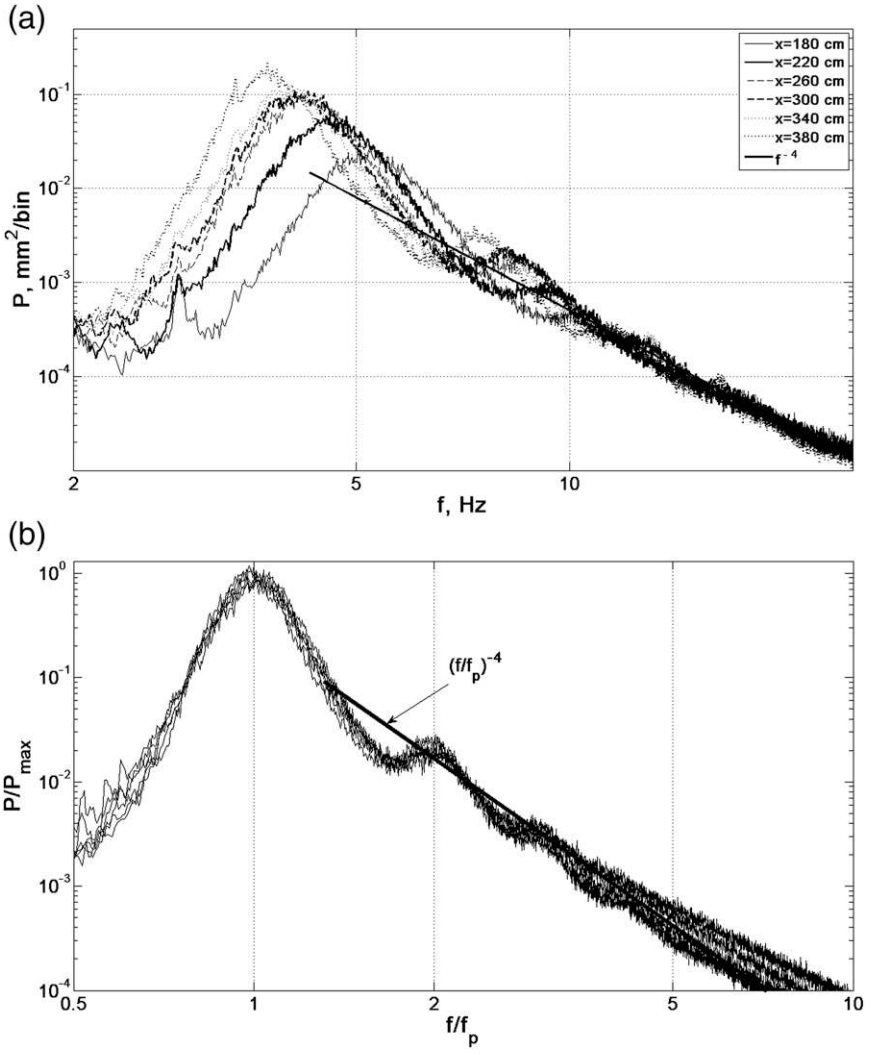

FIG. 10. The power spectrum of the surface elevation for (a) different fetches at $U_{\max} = 6.6$ m s^{-1} and (b) various wind velocities at $x = 260$ cm.

the spectral width decreases with x, the rate of decrease is higher at lower fetches and wind velocities. The values of the spectral width at wind velocities $U_{\max} > 5.5$ m s^{-1} and fetches exceeding about 200 cm seem to be less dependent on the airflow rate and decrease somewhat with fetch from around $\nu = 0.17$ at $x = 220$ cm to about $\nu = 0.145$ at $x = 380$ cm. The process of generation of water waves by wind is thus characterized by decrease in both the peak frequency f_p and the spectral width ν. As discussed by Liberzon and Shemer (2011), waves at various frequencies are excited by wind at lower fetches; the lower frequency harmonics grow in amplitude under the action of wind along the test section, while waves with higher frequencies attain their maximum saturation amplitudes faster and then decay gradually. Higher winds cause a more rapid evolution of the wave field manifested by significantly smaller spectral widths at shorter fetches.

The values of ν characterize the spectral shape at lower frequencies around f_p. A closer look at the power law behavior of the high-frequency spectral tail is presented in Fig. 12 that is plotted in normalized coordinates as in Fig. 10.

The high-frequency ''tail'' of the spectra shows the power-law dependence on frequency:

$$P/P_p = C(f/f_p)^{-n}. \tag{17}$$

The power n defined by the slope of the linear fit in Fig. 12 increases with fetch from $n = 3.1$ for $x = 100$ cm to $n = 3.74$ for the longest fetch, $x = 380$ cm. The solid line representing the ''-4 power law'' is also plotted for

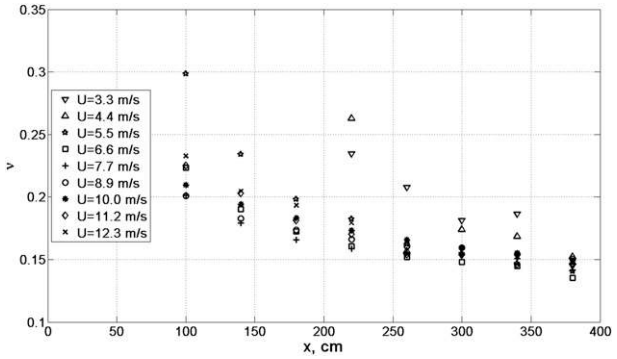

FIG. 11. Variation of the spectral width ν along the tank.

comparison. The fit range was chosen as from $3 < f/f_p < 6$, as the spectra in this part are free of noticeable higher harmonic peaks which can affect the slope.

The values of C and n of the high-frequency tail part of the spectrum retrieved from the fit (17) are summarized in Fig. 13. Only measurements performed at airflow rates corresponding to $U_{\max} \geq 6.6$ m s^{-1} were considered. The values of n plotted as a function of wave-age in Fig. 13a seem to follow a common trend growing monotonically with wave age from $n = 3$ to about $n = 4$ for more mature waves at larger fetches and relatively low wind velocities, thus attaining the typical value for the fully developed sea (Toba 1973; Badulin et al. 2007). The coefficients C in (17) presented in Fig. 13b are scattered around the value of 0.1, the scatter of data seems to decrease with wave age.

The deviation of the random wind wave field from Gaussianity can be characterized by coefficients of skewness λ_3 and kurtosis λ_4 defined as

$$\lambda_3 = \overline{\eta^3}/(\overline{\eta^2})^{3/2}, \quad \lambda_4 = \overline{\eta^4}/(\overline{\eta^2})^2. \tag{18}$$

For a normally distributed random wave field, $\lambda_3 = 0$ and $\lambda_4 = 3$. The calculated from the measured data values of λ_3 and λ_4 for all cases are presented in Figs. 14 and 15. The skewness coefficient λ_3 characterizes the vertical wave asymmetry; it is positive for all records and demonstrates a general trend to increase with fetch and with wind velocity, attaining values close to 0.5 at larger fetches and wind velocities. These results are in agreement with measurements of wind waves in a laboratory tank by Huang and Long (1980). The second-order bound waves that cause effective increase in wave crests and decrease in troughs constitute the dominant contribution to λ_3 (Shemer et al. 2010a). According to Tayfun (2006), the skewness coefficient in a narrowband wave field due to second-order bound waves has an upper limit that equals to wave steepness multiplied by 3. Comparison of Figs. 14 and 8a indicates that the measured values of λ_3, while indeed increasing with the wave steepness ε as expected, tend to exceed somewhat the Tayfun's limiting values of 3ε. This observation is in agreement with the results of Shemer and Sergeeva (2009) for a narrow-banded unidirectional wavemaker-generation random wave field.

The kurtosis coefficient λ_4 plotted in Fig. 15 is below the Gaussian value of 3 for all wind velocities and at all fetches, except for the low wind velocity at moderate fetches where it is slightly above that value. For wind velocities exceeding about 7 m s^{-1}, the kurtosis coefficient seems to be nearly constant, with λ_4 being in the range 2.4–2.6 and essentially independent of both the fetch and the wind velocity. These values of λ_4

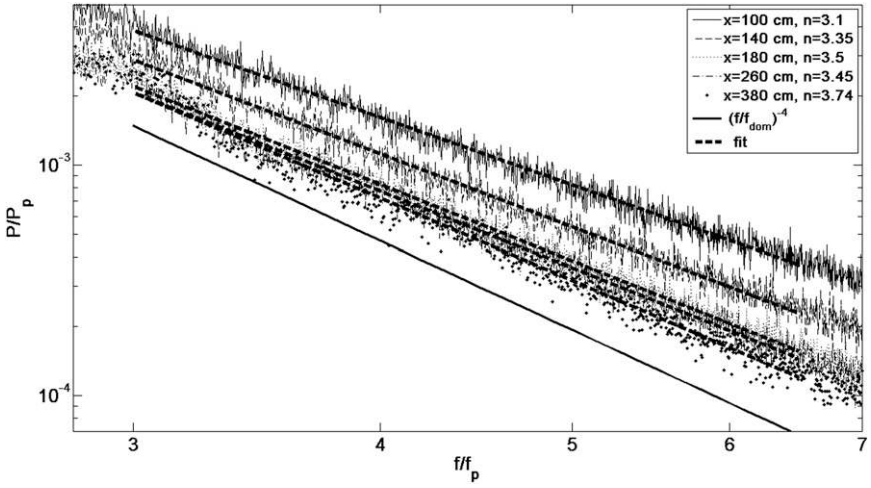

FIG. 12. High-frequency part of the surface elevation power spectrum for $U_{\max} = 8.9$ m s^{-1} and various fetches.

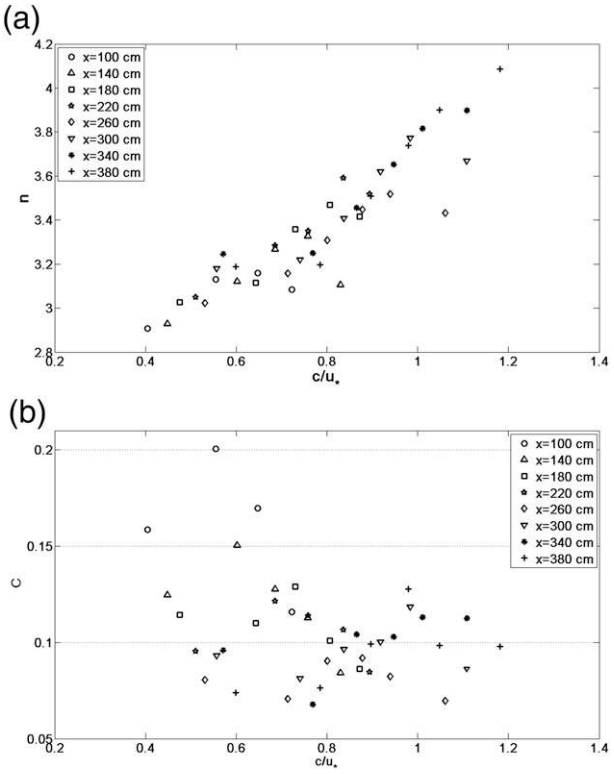

FIG. 13. (a) The power n as a function of wave-age and (b) coefficient of proportionality as a function of wave-age.

indicate at a relative deficit of large amplitude waves in the distribution. The values of kurtosis in Fig. 15 are in qualitative agreement with Huang and Long (1980), as well as with the experimental results of Shemer et al. (2010a,b) obtained for mechanically generated unidirectional random waves at comparable values of the spectral width ν. They disagree, however, with the results of wind wave simulations by Annenkov and Shrira (2009) based on the Zakharov equation who reported on $\lambda_4 > 3$.

The conjecture regarding the relatively low probability of very steep waves in the present experiments, deduced from the results of Fig. 15, is further validated by plotting the probability distribution of the wave height along the flume in Fig. 16. The results presented for the extreme values of the airflow rate in these experiments are representative also for all other wind velocities. For linear narrow-band Gaussian waves, Longuet-Higgins (1952) demonstrated that the distributions of the wave heights H tend to follow the Rayleigh exceedance distribution

$$F(H) = \exp\left(-\frac{H^2}{8\overline{\eta^2}}\right). \tag{19}$$

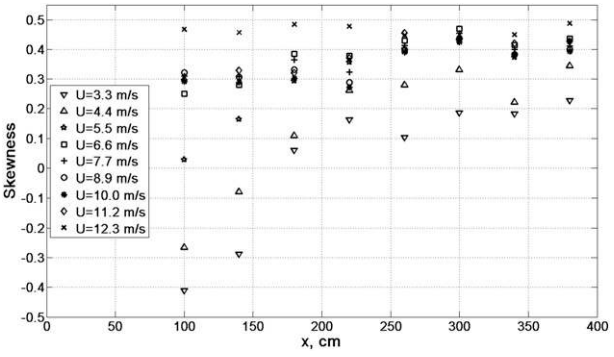

FIG. 14. The skewness coefficient λ_3.

Longuet-Higgins (1963) also has shown that nonlinearities can cause the deviation of surface elevation distributions $F(H)$ from the Gaussian statistics and approximated $F(H)$ by a Gram-Charlier expansion. Huang and Long (1980) carried out a comparison of the experimentally measured wind waves' height distributions with the Longuet-Higgins (1963) model and obtained a reasonable agreement between their results and the theory, although some problems in application of the Gram-Charlier approximation called for additional studies. Later, Tayfun and Fedele (2007) suggested coupling of the Gram-Charlier expansion with the Tayfun (1980, 2006) model for narrow-banded sea.

In Fig. 16 the exceedance distributions obtained in the present experiments are compared with the Rayleigh distribution as well as with the 3rd order Tayfun and Fedele (2007) model (TF3). For all experimental conditions, notable deviations from the Rayleigh distribution are indeed clearly visible in this Figure. For the Rayleigh distribution, the significant wave height $H_s \approx 4(\overline{\eta^2})^{1/2}$. The probability of small and moderate waves with heights $H < H_s$, is higher in Fig. 16 than that corresponding to the Rayleigh distribution. The probability of waves higher than H_s, however, is overestimated by

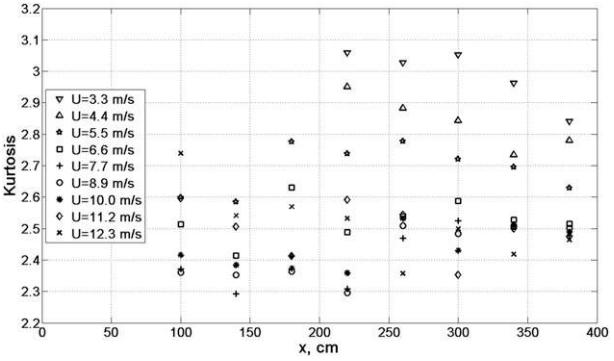

FIG. 15. The kurtosis coefficient λ_4.

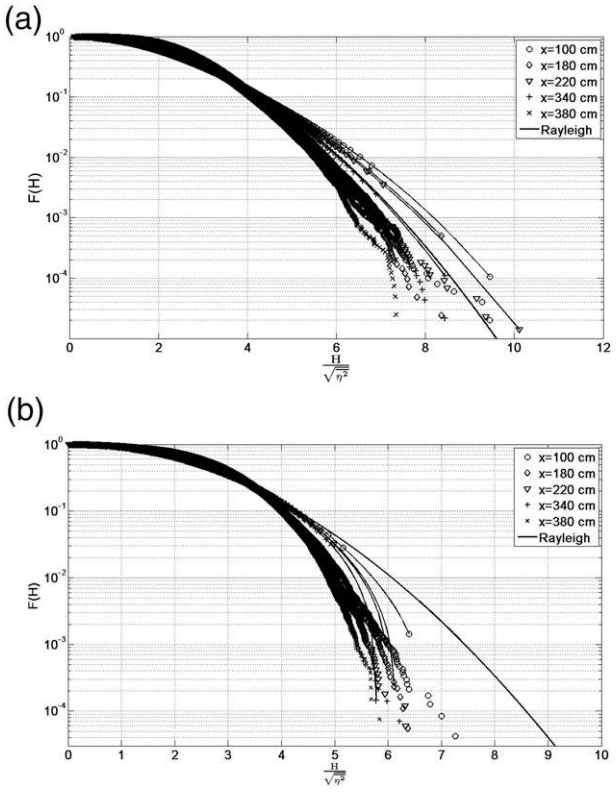

FIG. 16. Probability distribution for wave heights: (a) $U_{\max}$ = 3.3 m s^{-1} and (b) $U_{\max}$ = 12.3 m s^{-1}. Solid curves with markers denote the TF3 distributions at corresponding fetches.

(19). These deviations from the Rayleigh distribution are stronger for the higher wind velocity in Fig. 16b as compared to the weaker wind case in Fig. 16a. The experimental data obtained here compare qualitatively well with the TF3 model for all examined wind speeds, especially for small and moderate heights. The quantitative agreement improves with the increase in wind speed and at longer fetches as the waves become longer (Fig. 16b). No dependence of the measured $F(H)$ on fetch can be clearly identified in Fig. 16. Several extreme waves recorded at the low wind flow rate appear exclusively at short fetches characterized by very small wave heights. Extremely steep (the so-called freak) waves are usually defined as waves with heights exceeding $2H_s$ or $8(\overline{\eta^2})^{1/2}$. It thus follows from the present results that the probability of such waves is considerably overestimated by (19). The freak waves are totally absent in all ensembles accumulated at the high wind velocity, Fig. 16b.

4. Discussion and conclusions

A random quasi-steady wave field evolving in a small-scale wind wave flume was studied. Compared to field studies, laboratory experiments offer an obvious considerable advantage of accurate control of flow conditions, repeatability, and possibility of detailed and extended measurements under steady conditions. To assess the relevance of experiments in a small flume, the extent of similarity between waves excited in such laboratory facility and wind-generated waves in the sea was examined. For that purpose extended and statistically significant temporal records of instantaneous water surface fluctuations under variety of steady wind forcing conditions and at numerous fetches along the flume were accumulated. Statistical and spectral parameters of the wave field evolving along the test section were compared with the available theoretical and experimental data accumulated during both laboratory and field studies. Spectral integral moments were used to calculate the characteristic wave amplitudes and frequencies, as well as the spectral widths. The appropriate dimensionless parameters governing wind water waves' excitation and evolution were considered to enable comparison between the results obtained investigating wave fields in laboratory and in the sea, as those differ notably by their spatial and temporal scales. Relations between such parameters in the present experimental facility were obtained and compared with available data derived on the basis of laboratory and field studies. Finally, a statistical characterization of wave heights distribution was evaluated by calculating skewness and kurtosis coefficients, as well as the wave height exceedance distributions.

Wave energy growth with fetch was documented for a range of wind speeds. The friction velocity u_* was used as a characteristic wind velocity being a more natural characteristic in the laboratory facility than the U_{10} velocity often used in the field measurements. Relation between the dimensionless characteristic surface elevation amplitude and the dimensionless peak frequency depicted in Fig. 4 corresponds to power law with the power value of -1.87, not very different from the empirical value of -1.5 suggested by Toba (1972) on the basis of field data analysis. The wave amplitude growth with the dimensionless fetch observed in the present experiments and summarized in Fig. 5 is also in good agreement with the available laboratory results by Mitsuyasu and Honda (1974), Mitsuyasu (1968), as well as the field observations (Kahma 1981; Hasselmann et al. 1980). The agreement becomes less impressive for lower wind velocities, $U_{\max} < 7$ m s^{-1}, where the wave field is characterized by wide-band waves of very small amplitudes, so the results are less reliable and exhibit considerable scatter.

The power spectra were obtained by averaging a large number of statistically independent estimates, taking

advantage of steady conditions in the experimental facility. The averaged spectra for each fetch and wind velocity covered up to 5 decades. Two spectral domains, the high-frequency tail, and the vicinity of the spectral peak, were treated separately. To estimate the spectral tail behavior care was taken to consider frequencies exceeding about $3.5f_p$. At those frequencies the direct effect of bound waves on the spectral shape is not discernible anymore, see Figs. 10 and 12; it thus can be assumed that the slope represents mainly the contribution of free waves. This distinction allows carrying out comparison of the present results with theoretical estimates based on considering free waves only—see, for example, Badulin et al. (2007). The spectral tails dependence on frequency was found to follow the power law (17) with n about 3 at lower wave ages and then increasing with c/u_*, but generally remaining somewhat below the values of $n = 4$ suggested by Toba (1973) and Badulin et al. (2007). The exponents n attain the value of $n = 4$ in the present study only at the largest wave ages. It should be stressed, however, that those wave ages correspond to the very small wind waves at shorter fetches and lower wind velocities; as stressed above, the results at these conditions are less accurate. Moreover, the waves at the frequency range considered are strongly affected by surface tension, while Badulin et al. (2007) consider pure gravity waves. The values of the coefficient C in the power relation (17) presented in Fig. 13b are also close to $C = 0.1$ suggested by Toba. It thus can be concluded that the behavior of the high frequency spectral tail in the present experiments does not differ significantly from that obtained in the previous theoretical and field studies.

The frequency domain around the spectral peak frequency was analyzed separately. Dimensionless spectral width ν constitutes an integral property of this part of the spectrum, since it was calculated from spectral moments estimated for that domain, see (16). Excluding again very small waves at low wind velocities, the values of the spectral width decrease somewhat with fetch from about $\nu = 0.22$ at short fetches to about $\nu = 0.15$ for higher fetches and stronger winds (Fig. 11). It should be stressed that for fetches longer than about 180 cm and wind speeds higher than 7 m s^{-1} the spectral width is virtually independent of wind velocity for a given fetch, the scatter of a few percent being within the accuracy of measurements. The observed decrease in both the peak frequency and the spectral width with the increasing wind speed, or with fetch, is characteristic for random wind-generated waves, where higher frequency components grow initially more rapidly with their amplitudes attaining saturation that is followed by gradual decay, while lower frequency components maintain

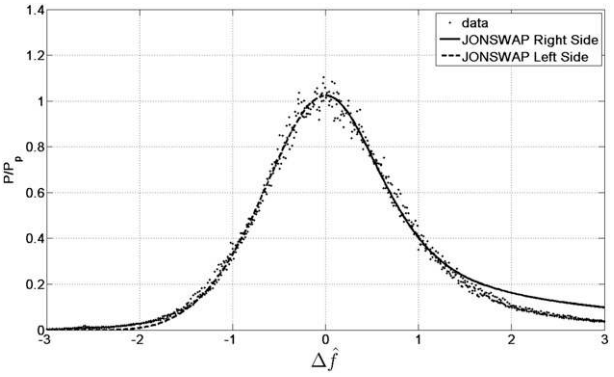

FIG. 17. Averaged over all fetches exceeding 100 cm normalized power spectra as a function of $\Delta\hat{f}$ and the fitted JONSWAP shape.

exponential growth with fetch Liberzon and Shemer (2011), Goda (2000), and Janssen (2004). The similarity of normalized spectral shapes around the peak frequency as shown in Fig. 10b and the essential independence of the spectral width of the airflow rate at a fixed fetch suggests introduction of normalized frequency deviation from the peak value $\Delta\hat{f}$ defined as

$$\Delta\hat{f} = \frac{1}{\nu}\left(\frac{f}{f_p} - 1\right). \tag{20}$$

The normalized spectra for all fetches exceeding $x = 100$ cm and maximum wind velocities $U_{\max} > 7$ m s^{-1} plotted in Fig. 17 for the range of $-3 < \Delta\hat{f} < 3$ collapse on a single curve. It is thus instructive to compare this spectral shape with a standard JONSWAP spectrum based on extensive measurements in the North Sea. Following Goda (2000), this spectral shape can be written as

$$P = \beta H_S^2 T_p (f/f_p)^{-5} \exp\left[-\frac{5}{4}\left(\frac{f}{f_p}\right)^{-4}\right] \gamma^{\exp[-(f/f_p-1)/2\sigma^2]}, \tag{21}$$

where γ is a peak enhancement coefficient, σ has separate values σ_R and σ_L for the right and the left sides of the spectrum, β is a coefficient that defines the peak power of the spectrum, so that the peak value

$$P_p = \beta H_S^2 T_p. \tag{22}$$

In the variables of Fig. 17, (21) takes form of

$$\frac{P}{P_p} = (1 + \nu\Delta\hat{f})^{-5} \exp\left[-\frac{5}{4}(1 + \nu\Delta\hat{f})^{-4}\right] \gamma^{\exp[-(\nu\Delta\hat{f}/\sqrt{2}\sigma)^2]}. \tag{23}$$

The spectral shape (23) was therefore fitted to the data plotted in Fig. 17. The coefficients γ, σ_R, and σ_L were

obtained from this fit for each fetch using the corresponding dimensionless spectral widths ν averaged over wind velocities, see Fig. 11. The fitted shapes are in a good agreement with the data at both sides of the peak value $\Delta\hat{f} = 0$. The values of γ remain nearly constant at about $\gamma = 3.58$ for all fetches. The coefficients $\sigma_R \approx 0.136$ and $\sigma_L \approx 0.148$ were also essentially independent of fetch. In view of insensitivity of the coefficients of (23) to fetch and wind velocity, a single dimensionless normalized JONSWAP-type spectrum averaged over all fetches, and using averaged value of $\nu = 0.173$, is plotted in Fig. 17. The spectrum was then also fitted with the JONSWAP shape presented by (23), yielding values of $\gamma = 3.573$, $\sigma_R = 0.133$, and $\sigma_L = 0.143$ representative for all included experimental conditions. The resulted fit curves are also plotted in Fig. 17.

A very good agreement was obtained for the longer waves at the left side of the spectrum; the fit for the higher frequency part of the spectrum deviated slightly from the experimental data starting from about $\Delta\hat{f} > 1.4$. The value of γ, expressing the sharpness of the spectral peak, is similar to $\gamma = 3.3$ reported for mature waves in the North Sea (JONSWAP) experiments Hasselmann et al. (1980). The coefficients σ obtained for the present experimental data that characterize spectral shape steepness, however, were somewhat higher than those generally accepted for the JONSWAP spectrum, that is, $\sigma_R \approx 0.09$ and $\sigma_L \approx 0.07$.

The peak power of the JONSWAP spectrum is determined by the coefficient β, see (22). Values of β calculated from the measured spectra using significant wave heights H_S presented in Table 2 are plotted in Fig. 18 as a function of wave age. Calculation for the value of γ obtained in the present study according to Goda (2000) yields $\beta \approx 0.21$. Figure 18 demonstrates that for all experimental conditions except of high values of $\hat{x}$ that correspond to the lowest wind velocities and undeveloped wind wave field, the measured peak energy coefficients β were found to be mostly slightly above $\beta = 0.2$ and very close to the computed according to Goda value.

Next, the waves shape and the surface elevation probability distributions were also compared with the corresponding values characterizing sea waves. Steepness of the dominant waves component, ε, grew with the increase in $U_{\max}$, while its dependence on fetch quickly diminishes (Fig. 8). At all experimental conditions values of ε did not exceed the apparent saturation value of about 0.2, constrained by wave energy dissipation that at the length scales characteristic for the present experiments is mainly due to microbreaking and the appearance of parasitic ripples, see Caulliez et al. (2008). For stronger winds the wave steepness

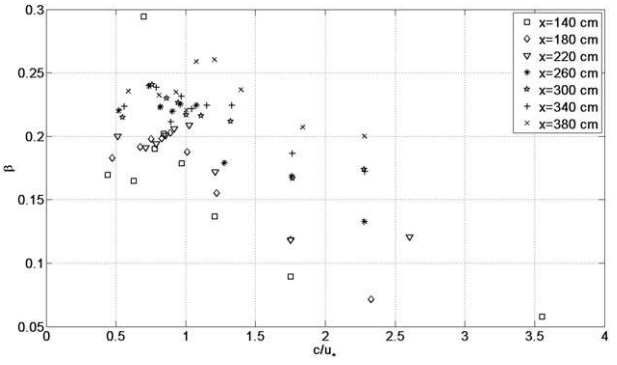

FIG. 18. The peak energy coefficient β in the JONSWAP spectrum as a function of c/u_*.

remained virtually constant and independent of fetch and wave age, see Fig. 8a. Although the dissipation mechanism in the present experiments may differ from that in the open sea, the limiting value of the wave steepness was found to be similar to the one observed in field measurements.

Deviations of the surface elevation variation from that corresponding to Gaussian were examined using higher distribution moments of skewness λ_3 and kurtosis λ_4, see (20). The wave height exceedance distribution was compared with the Rayleigh distribution. For all experimental conditions values of λ_3 were positive and in general agreement with the theoretical estimates of Tayfun (2006) and the experimental results of Shemer and Sergeeva (2009) for a narrow-banded random wave field. Values of kurtosis coefficient λ_4 were below 3, indicating relative deficit in large amplitudes in the ensemble, in agreement with the findings of Shemer et al. (2010a) for unidirectional mechanically generated random waves studied in a very large experimental wave tank. The low kurtosis values suggested that the deviation from Gaussian distribution of wave heights probability can be expected. Indeed deviation from Rayleigh distribution for all experimental conditions was obtained for all experimental conditions (Fig. 16). While the probability of relatively small waves was higher than that corresponding to the Rayleigh distribution, the probability of very high waves was vanishingly small. The experimental results showed good qualitative agreement with the TF3 model of broad banded wind waves heights distribution. Quantitative agreement with the TF3 model improves for higher wind speeds and at longer fetches and thus longer waves dominating the wave field; these conditions correspond to narrower surface elevation spectra (Fig. 10). Results obtained for waves driven by wind-induced stresses are again in agreement with Shemer et al. (2010a) who demonstrated that for surface stress-free wavemaker-generated waves

with relatively broad spectra, the probability of the so-called freak waves is virtually zero.

To conclude, extensive statistical characteristics of wind-generated waves were accumulated in the present experiments carried out in a small experimental facility. The results are presented using appropriate dimensionless parameters, thus enabling detailed comparison with the available data obtained either in larger experimental installations, mostly in the absence of wind, or during field measurements. In particular, a dimensionless spectral form for the energy containing domain around the peak wave frequency was suggested allowing direct quantitative comparison of numerous spectra obtained at various conditions. Strong similarity was obtained between the present results and those obtained in the open sea. The presented study thus demonstrates that in spite of certain limitations imposed by size, experimental research on wind generated water waves in relatively small experimental facilities may yield valuable results, applicable at considerably larger scales. Experiments in small- and midsize laboratory facilities, beyond being relatively inexpensive, have significant benefits as they allow detailed investigation of diverse processes associated with the generation of water waves by wind under repeatable conditions in a controlled environment and with temporal and spatial resolutions that cannot be achieved during field measurements.

Acknowledgments. The authors gratefully acknowledge support of this study by the Israel Science Foundation under Grant 153/11. We also acknowledge the help offered by Dr. A. Sergeeva.

REFERENCES

Annenkov, S. Y., and V. I. Shrira, 2009: Evolution of kurtosis for wind waves. *Geophys. Res. Lett.,* **36,** L13603, doi:10.1029/2009GL038613.

Badulin, S. I., A. V. Babanin, V. E. Zaharov, and D. Resio, 2007: Weakly turbulent laws of wind wave growth. *J. Fluid Mech.,* **591,** 339–378.

Caulliez, G., V. Makin, and V. Kudryavtsev, 2008: Drag of the water surface at very short fetches: Observations and modeling. *J. Phys. Oceanogr.,* **38,** 2038–2055.

Forristall, G. Z., 1978: On the statistical distribution of wave heights in a storm. *J. Geophys. Res.,* **83,** 1548–1552.

——, 2005: Understanding rogue waves: Are new physics really necessary? *Rogue Waves: Proc. 14th 'Aha Huliko'a Hawaiian Winter Workshop,* Honolulu, HI, University of Hawaii at Manoa, 29–35.

Fu, L.-L., and R. Glazman, 1991: The effect of the degree of wave development on the sea state bias in radar altimetry measurement. *J. Geophys. Res.,* **96** (C1), 829–834.

Goda, Y., 2000: *Random Seas and Design of Marine Structures.* World Scientific, 443 pp.

Hasselmann, D. E., M. Dunckel, and J. A. Ewing, 1980: Directional wave spectra observed during JONSWAP 1973. *J. Phys. Oceanogr.,* **10,** 1264–1280.

Huang, N. E., and S. R. Long, 1980: An experimental study of the surface elevation probability distribution and statistics of wind generated waves. *J. Fluid Mech.,* **101,** 179–200.

Janssen, P. A. E. M., 2004: *The Interaction of Ocean Waves and Wind*. Cambridge University Press, 300 pp.

Kahma, K. K., 1981: A study of the growth of the wave spectrum with fetch. *J. Phys. Oceanogr.,* **11,** 1503–1515.

——, and C. J. Calkoen, 1992: Reconciling discrepancies in observed growth of wind-generated waves. *J. Phys. Oceanogr.,* **22,** 1389–1405.

Kinsman, B., 1965: *Wind Waves*. Prentice-Hall, Inc., 676 pp.

Kitaigorodskii, S. A., 1961: Application of the theory of similarity to the analysis of wind generated wave motion as a stochastic process. *Izv. Akad. Nauk SSSR, Ser. Geofiz.,* **1,** 105–117.

Liberzon, D., and L. Shemer, 2011: Experimental study of the initial stages of wind waves' spatial evolution. *J. Fluid Mech.,* **681,** 462–498.

Longuet-Higgins, M., 1952: On the statistical distribution of the heights of sea waves. *J. Mar. Res.,* **11,** 245–266.

——, 1963: The effect of nonlinearities on statistical distributions in the theory of sea waves. *J. Fluid Mech.,* **17,** 459–480.

Mitsuyasu, H., 1968: On the growth of the spectrum of wind-generated waves I. *Rep. Res. Inst. Appl. Mech. Kyushu Univ.,* **16,** 459–482.

——, and T. Honda, 1974: The high frequency spectrum of wind-generated waves. *J. Oceanogr. Soc. Japan,* **30,** 185–198.

Mori, N., M. Onorato, P. A. E. M. Janssen, A. R. Osborne, and M. Serio, 2007: On the extreme statistics of long-crested deep water waves: theory and experiments. *J. Geophys. Res.,* **112,** C09011, doi:10.1029/2006JC004024.

Onorato, M., A. R. Osborne, M. Serio, and L. Cavaleri, 2005: Modulational instability and non-Gaussian statistics in experimental random water-wave trains. *Phys. Fluids,* **17,** 078101, doi:10.1063/1.1946769.

——, ——, ——, ——, C. Brandini, and C. T. Stansberg, 2006: Extreme waves, modulational instability and second order theory: Wave flume experiments on irregular waves. *Eur. J. Mech.,* **25B,** 586–601.

——, and Coauthors, 2009: Statistical properties of mechanically generated surface gravity waves: A laboratory experiment in a three-dimensional wave basin. *J. Fluid Mech.,* **627,** 235–257.

Phillips, O. M., 1958: The equilibrium range in the spectrum of wind-generated waves. *J. Fluid Mech.,* **4,** 426–434.

——, 1977: *The Dynamics of the Upper Ocean*. 2nd ed. Cambridge University Press, 336 pp.

Pierson, W. J., and L. Moskowitz, 1964: A proposed spectral form for fully developed wind seas. *J. Geophys. Res.,* **69,** 5181–5190.

Shemer, L., and A. Sergeeva, 2009: An experimental study of spatial evolution of statistical parameters in a unidirectional narrow-banded random wavefield. *J. Geophys. Res.,* **114,** C01015, doi:10.1029/2008JC005077.

——, ——, and D. Liberzon, 2010a: Effect of the initial spectrum on the spatial evolution of statistics of unidirectional nonlinear random waves. *J. Geophys. Res.,* **115,** C12039, doi:10.1029/2010JC006326.

——, ——, and A. Slunyaev, 2010b: Applicability of envelope model equations for simulation of narrow-spectrum unidirectional random field evolution: Experimental validation. *Phys. Fluids,* **22,** C12039, doi:10.1063/1.3290240.

Socquet-Juglard, H., K. Dysthe, K. Trulsen, H. E. Krogstad, and J. Liu, 2005: Probability distributions of surface gravity waves during spectral changes. *J. Fluid Mech.,* **542,** 195–216.

Tayfun, M. A., 1980: Narrow-band nonlinear sea waves. *J. Geophys. Res.,* **85** (C3), 1548–1552.

——, 2006: Statistics of nonlinear wave crests and groups. *Ocean Eng.,* **33,** 1589–1622.

——, and F. Fedele, 2007: Wave height distributions and nonlinear effects. *Ocean Eng.,* **34,** 1631–1649.

Toba, Y., 1972: Local balance in the air-sea boundary processes. I. On the growth process of wind waves. *J. Oceanogr. Soc. Japan,* **28,** 109–120.

——, 1973: Local balance in the air-sea boundary processes. III. On the spectrum of wind waves. *J. Oceanogr. Soc. Japan,* **29,** 209–220.

Zavadsky, A., and L. Shemer, 2012: Characterization of turbulent air flow over evolving water-waves in a wind wave tank. *J. Geophys. Res.,* **117,** C00J19, doi:10.1029/2011JC007790.